Acta Metallurgica Sinica (English Letters)
https://doi.org/10.1007/s40195-022-01465-9

Enhanced Fatigue Properties of 2219 Al Alloy Joints via Bobbin Tool Friction Stir Welding

Zhenlin Wang[1,2] · Beibei Wang[1] · Zhen Zhang[1] · Peng Xue[1,2] · Yunfei Hao[3] · Yanhua Zhao[3] · Dingrui Ni[1,2] · Guoqing Wang[4] · Zongyi Ma[1,2]

Received: 17 June 2022 / Revised: 13 July 2022 / Accepted: 25 July 2022

Abstract
In the present study, 2219-T87 Al alloy plates, 4 mm in thickness, were subjected to bobbin tool friction stir welding (BT-FSW) under relatively high welding speeds of 200 and 400 mm/min, with the aim to analyze the effect of welding speeds on fatigue properties of the joints. The results showed that the tension–tension high-cycle fatigue performance of the BT-FSW joints at room temperature was significantly enhanced compared to that of other joints of 2xxx series Al alloys counterparts. Particularly at a high welding speed of 400 mm/min, the fatigue strength of the joint reached 78% of the base material together with a high tensile strength of 311 MPa. It was found that the joint line remnants had no effects on the fatigue properties of the BT-FSW joints due to the elimination of root flaws under the action of the lower shoulder. Most of the samples with the welding speed of 200 mm/min failed at the thermo-mechanical zone (TMAZ) during fatigue tests, attributable to the coarsened grains and precipitates, but all of the samples with high welding speed of 400 mm/min randomly failed at the nugget zone due to the improved hardness value in the TMAZ.

Keywords 2219 Al alloys · Bobbin tool friction stir welding · Microstructure · Fatigue properties

1 Introduction

2xxx series Al alloys, due to their characteristics of lightweight and high strength, are widely used in aerospace field especially in aircraft skin, fuel storage tank, and key structural member. However, for the fusion welding of 2xxx series Al alloys, the poor solidification microstructure (branch crystal, segregation) and porosity are unavoidable, resulting in reduced mechanical properties. Friction stir welding (FSW), known as a solid-state joining technique, has been widely used in welding such alloys, because the above problems in traditional fusion welding can be effectively avoided in FSW joints [1, 2].

However, there are still some problems in the practical application of FSW. For conventional FSW with a single shoulder, the rigid backing plate under the workpiece is indispensable for sustaining the high downforce and preventing the deformation of the workpiece, which limits the application of conventional FSW in curved and hollow structures. In order to avoid these problems, bobbin tool friction stir welding (BT-FSW) is applied because of the particularity of its double-shoulder structure, whose lower shoulder can effectively provide support component and avoid the formation of root flaw [3, 4].

During BT-FSW, complex heating and material flow were generated, resulting in unique microstructure and mechanical properties of the joints compared with the conventional FSW process [5]. The cross-sectional macrostructure of the BT-FSW joints was usually characterized

Available online at http://link.springer.com/journal/40195.

✉ Beibei Wang
bbwang@imr.ac.cn

✉ Dingrui Ni
drni@imr.ac.cn

1 Shi-Changxu Innovation Center for Advanced Materials, Institute of Metal Research, Chinese Academy of Sciences, Shenyang 110016, China

2 School of Materials Science and Engineering, University of Science and Technology of China, Shenyang 110016, China

3 China Academy of Launch Vehicle Technology, Beijing 100076, China

4 Capital Aerospace Machinery Company, Beijing 100076, China

Published online: 21 September 2022

by a symmetrically deformed dumbbell shape with uniform microstructure, which was related to the sufficient material flow induced by both the upper and lower shoulders. On the other hand, it is difficult to dissipate heat from the backing plate because the lower shoulder also generates a large amount of heat during the BT-FSW process [6]. Therefore, the mechanical properties of BT-FSW joints are mostly lower than those of the conventional FSW joints due to the severe softening [7]. The joint softening of 2219 Al alloy was mainly dependent on the precipitate distribution. The major strengthening precipitates of 2219 Al alloy are θ'' and θ' phases, which are metastable phases with cubic structures [8, 9]. The excessive heat during BT-FSW usually caused the dissolution, coarsening, and reprecipitation of the strengthening precipitates, which could lead to a significant reduction in joint strength.

In order to improve the mechanical property of BT-FSW joints, increasing the welding speed is a principal method to reduce the dissolution or coarsening of the precipitates according to the conventional FSW of Al alloys [10]. Regrettably, the welding speed of BT-FSW was usually no higher than 150 mm/min in the previous studies [3, 11, 12]. Hence, investigation on the mechanical properties of the BT-FSW joints at higher welding speed is necessary and meaningful.

However, the mechanical properties, especially the fatigue property, of BT-FSW joints with fast welding speed still remain unclear. Fatigue property is very important in industrial applications, which is always treated as the final criterion for the application of a new welding structure. Usually, the fatigue property of welding structure can be affected by microstructure and internal defects of the joints. It was reported that FSW joints had better fatigue performance compared with conventional fusion welded joints due to the reduced solidification defects [13]. For a sound FSW joint of Al alloys without void and tunnel defects, the joint line remnant (JLR) or the so-called S line is an important characteristic microstructure which can affect the fatigue properties [14–17].

Actually, the JLR is the oxidation products originating from the butt surfaces, which are broken and rearranged by the stirring effect during the welding process [18–20]. The morphologies of JLRs are most likely a mass of hard oxide particles [12] which imply that initial interfaces may not be fully welded [21], causing the earlier crack initiation and rapid crack propagation during fatigue deformation process. Zhou et al. [15] reported that for conventional FSW joints, the JLR caused a reduction for the crack initiation life under a cyclic loading and shortened the total fatigue life in a large degree. However, the root flaw is usually connected with the JLR in their study due to the lack of penetration in conventional FSW, which could be fatal to fatigue performance of joints as a prior site of crack initiation [22–27]. Jolu et al. [28] found that root flaws led to a 17% reduction of fatigue strength compared with that of the sound joints, even the FSW joints undergone a weld root polishing.

Obviously, the frequent coexistence between JLRs and root flaws brings out significant effect on the mechanical properties of the conventional FSW joints, especially for the fatigue properties. For the BT-FSW joints, root flaws can be eliminated due to the existence of the lower shoulder. In theory, fatigue properties should not be reduced or even be improved in the BT-FSW joints compared to that of the conventional FSW joints, even though more heat input was involved in the BT-FSW process. However, few attentions were paid to the JLR effect on the fatigue properties of the BT-FSW joints, especially for the 2xxx series Al alloy joints with higher welding speeds.

In the study, 2219-T87 Al alloy plates were subjected to BT-FSW under an optimized rotation rate of 300 r/min and the relatively high welding speeds of 200 and 400 mm/min, with the aim to clarify the influence of the JLR on the high-cycle fatigue (HCF) properties of the BT-FSW joints, so that to provide a more effective welding method for the 2xxx series Al alloys used in complicated structures.

2 Experimental

4-mm-thickness plates of 2219-T87 Al alloy with a length of 450 mm and a width of 150 mm were selected as base material (BM), which were butt BT-FSWed along the rolling direction, under a constant rotational rate of 300 r/min and welding speeds of 200 and 400 mm/min, as shown in Fig. 1. The H13 steel welding tool with both upper and lower shoulders 18 mm in diameter and a cylindrical threaded pin 8 mm in diameter was selected in this study. The chemical composition of the 2219-T87 Al alloy is presented in Table 1. For the sake of simplicity, the joints under different welding parameters were expressed in a brief form. For example, sample 300–200 denotes that the joint was finished at a

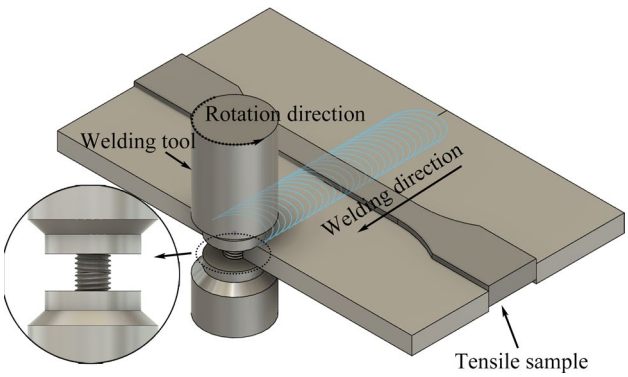

Fig. 1 Schematic illustration of BT-FSW and the sample locations for fatigue tests

Table 1 Chemical composition of 2219-T87 Al alloy

Material	Chemical composition (wt%)								
	Cu	Mn	Fe	Zr	Si	Ti	Zn	Mg	Al
2219-T87 Al	6.36	0.30	0.15	0.12	0.05	0.05	0.02	< 0.02	Bal.

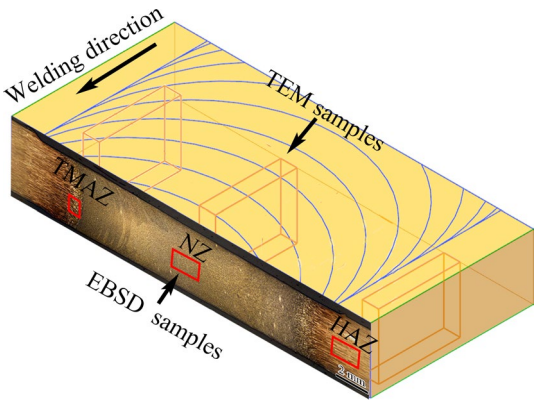

Fig. 2 Schematic illustrations of the sample locations for EBSD and TEM observations

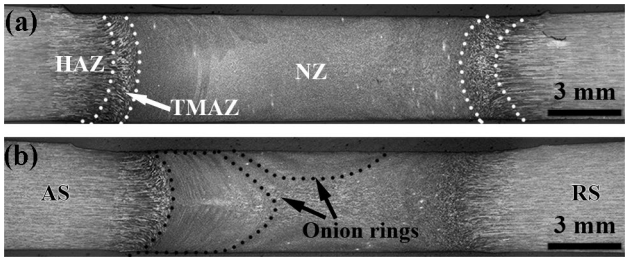

Fig. 3 Cross-sectional morphologies of BT-FSW 2219-T87 Al alloy joints under welding speeds of **a** 200 mm/min, **b** 400 mm/min

rotational rate of 300 r/min and a welding speed of 200 mm/min. All the joints were naturally aged at room temperature for more than 2 months before the microstructural observation and mechanical tests.

To observe the macrostructure by optical microscopy (OM), the cross-sectional samples (perpendicular to the welding direction) of the joints cut by electrical discharge machining were ground (with SiC sandpaper up to 2000 grit), polished, and etched by Keller reagent (2 mL HF + 3 mL HCl + 5 mL HNO_3 + 190 mL H_2O) for 20–30 s. Furthermore, in order to observe the morphologies of JLRs more clearly, the cross-sectional samples after mechanical tests were firstly etched by 2% NaOH solution for 20 min and then wiped gently with cotton dipped in a 20% nitric acid solution. The microstructural characterizations were carried out by electron backscattered diffraction technique (EBSD) and transmission electron microscopy (TEM), and the samples were cut from the corresponding locations in the welds using an electrical discharge machine, as shown in Fig. 2. EBSD specimens were ground and then electro-polished in a solution of 10 ml $HClO_4$ and 90 ml C_2H_5OH at 248 K under a potential of 12 V for 60 s. TEM foils were prepared by double-jet electrolytic polishing using a solution of 30 ml HNO_3 and 70 ml CH_3OH at 248 K under a potential of 12 V.

Vickers microhardness was measured on the cross section of the joints perpendicular to the welding direction on a Leco-LM-247AT hardness tester under a load of 500 g with a holding time of 13 s. The hardness contour maps were acquired by measuring 3 lines on the cross section with the interval of 1 mm between each other. In each line, 47 indentations with 1 mm spacing interval were measured.

The tensile and fatigue samples with a gauge length of 50 mm and a gauge width of 10 mm were machined perpendicular to the FSW direction. Uniaxial static tensile tests were tested using Instron 8801 tester at room temperature with an initial strain rate of 10^{-3} s^{-1}. The HCF tests were also conducted on carried the Instron 8801 tester at room temperature using a sinusoidal load-time function with a frequency of 30 Hz and a stress ratio of 0.1. All the samples were ground and polished before fatigue tests. The surface morphologies of the fractured samples after fatigue tests were characterized by Quanta-450 scanning electron microscopy (SEM).

3 Results and Discussion

3.1 Microstructure and Mechanical Properties

Figure 3 shows the cross-sectional macrostructure of the BT-FSW 2219-T87 joints under the welding speed of 200 and 400 mm/min, respectively. No porosity or tunnel defects were observed in the nuggets. Further, it should be noted that there were no root flaws in both joints due to the action of the lower shoulder. The cross section of joints can be divided into three classical subareas according to the morphology differences: nugget zone (NZ), thermo-mechanical affected zone (TMAZ), and heat-affected zone (HAZ). Different from the conventional FSW joints, a clearly extended NZ was observed in the BT-FSW joint even at a relatively high welding speed of 200 mm/min (Fig. 3a), due to the strong material flow under the effect of the lower shoulder [29]. In this case, the NZ of the 300–200 sample exhibited

an approximate rectangle shape and the width of the NZ can be comparable to the shoulder diameter.

With increasing the welding speed to 400 mm/min, the width of the NZ was slightly reduced due to the decrease in the heat input. Besides, the banded structure with dark and bright bands, well known as the "onion ring" in the conventional FSW joints [30], was formed in the NZ, as shown in Fig. 3b. However, due to the co-action of the double shoulders, the "onion ring" structure was not complete in the 300–400 sample, and distributed at the upper, lower, and advancing side (AS) parts of the NZ. Usually, the inhomogeneity of the "onion ring" structure has no significant effect on the mechanical properties, such as hardness or tensile property [31]. Compared with the NZ of conventional FSW, the disappeared or dispersive "onion ring" structure for the BT-FSW joints may be more beneficial to the mechanical properties including the HCF property, and this will be discussed in the next parts.

Figure 4 shows the EBSD microstructure of the NZ, TMAZ, and HAZ for each BT-FSW joint under different welding speeds. From the EBSD microstructure in Fig. 4a and d, uniform equiaxed grains were obtained in the NZs of both the BT-FSW joints. Obviously, dynamic recrystallization (DRX) occurred during BT-FSW process, which is similar to that of the conventional FSW process [32]. As the welding speed increased from 200 mm/min to 400 mm/min, the average grain size decreased from 4 to 3 μm in the NZs. Further, high fractions of high-angle grain boundaries (HAGBs) of 74% and 70% were achieved in 300–200 and 300–400 joints, respectively.

In the conventional FSW joints, the material in the TMAZ experienced thermal cycles and plastic deformation and usually exhibited an elongated a morphology [33]. However, DRX also occurred in the TMAZ of the 300–200 sample due to the large heat input from the double shoulders during the BT-FSW process, and no obvious elongated grains were observed (Fig. 4b). Compared with the 300–200 sample, the TMAZ experienced a lower heat input in the 300–400 sample, which was not high enough to induce the DRX, and therefore, the typical elongated grain morphology was observed, as shown in Fig. 4e. Different from the NZ and TMAZ, the HAZ was only suffered from the thermal cycle, leading to the coarsening of grains and precipitates [34]. The HAZs of both joints were characterized by the coarse and elongated grains which was a typical hot-rolled structure, as shown in Fig. 4c and f. The grains were obviously coarsened in the 300–200 sample compared with that of the 300–400 sample, due to the higher heat input under a relatively lower welding speed.

For precipitation-strengthened Al alloys, the precipitates are changed obviously during the welding process. It is well accepted that the aging precipitation sequence of a 2xxx series Al alloy is: SSSS → GP zone → θ'' → θ' → θ [35]. Due to the similar transformation characteristics of the precipitates in various zones of the conventional FSW and BT-FSW joints [36], only the precipitate morphologies of 300–200 sample were analyzed in detail via TEM, as shown in Fig. 5. The BM was characterized by densely distributed plate-like precipitates with lengths of 100–200 nm (Fig. 5a), which should be the metastable θ'

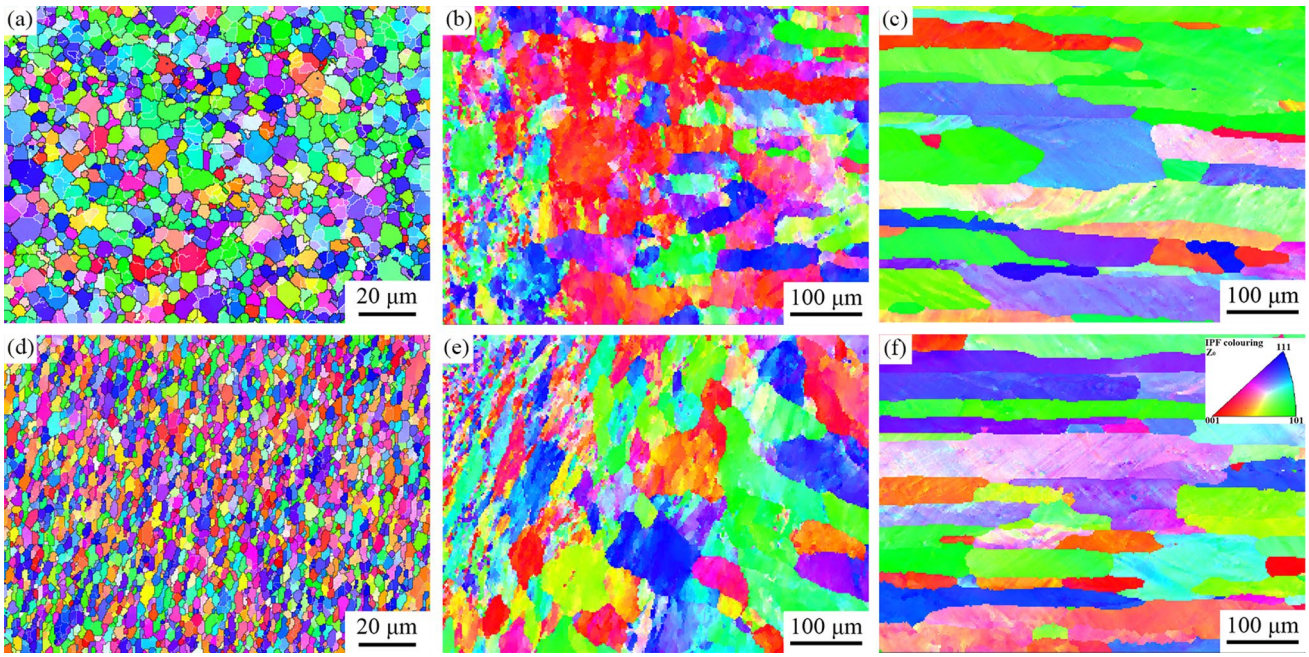

Fig. 4 Microstructures of the BT-FSW joints of 300–200 sample: **a** NZ, **b** TMAZ, **c** HAZ; 300–400 sample: **d** NZ, **e** TMAZ, **f** HAZ

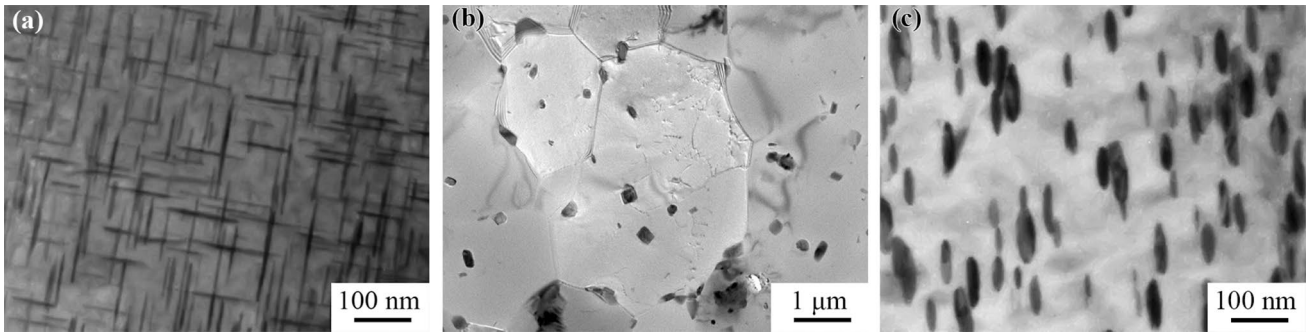

Fig. 5 Precipitate distribution of **a** BM and sample 300–200: **b** NZ, and **c** TMAZ

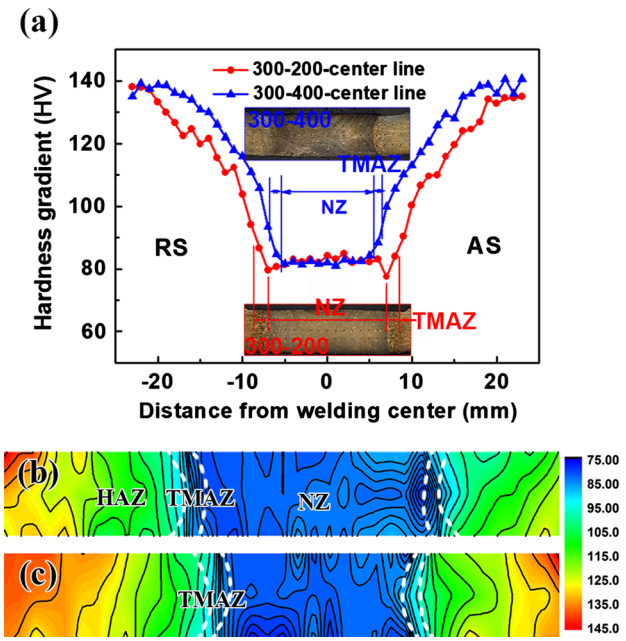

Fig. 6 **a** Microhardness distribution of transverse cross section along the center lines of BT-FSW joints and 2D hardness contour map under welding speeds of **b** 200 mm/min, **c** 400 mm/min

phase according to the previous investigations [37, 38]. In the NZ, the plate-like precipitates disappeared and only a few coarsened precipitates were observed, which exhibited the typical morphologies of the equilibrium θ phase [39]. Obviously, most of the precipitates were dissolved into the Al matrix due to the high temperature in the NZ and some non-dissolved precipitates were coarsened (Fig. 5a). Compared to that in NZ, the temperature in the TMAZ was lower, and thus, the precipitates cannot be dissolved and still remained the original plate-like morphologies. However, the precipitates were obviously coarsened, becoming shorter and wider, as shown in Fig. 5c.

The microhardness distribution maps of the BT-FSW joints are shown in Fig. 6. Two typical hardness profile characteristics, the W-shaped (300–200 sample) and the U-shaped (300–400 sample), were observed along the center line of the cross section in Fig. 6a. It is clear that obvious softening appeared in the weld zone compared to that in the BM with a high hardness value of ~ 137 HV. The lowest hardness zone (LHZ) was located at the TMAZ of 300–200 sample, and the hardness value was only ~ 78 HV, as shown in Fig. 6a and b. The hardness value of the NZ was slightly higher than that of the TMAZ, and the average hardness value was about 83 HV (Fig. 6b). The hardness value of the TMAZ was improved as increasing the welding speed to 400 mm/min, and even higher than that of the NZ. In this case, the whole NZ became the LHZ, as shown in Fig. 6c.

Table 2 Tensile properties of BM and BT-FSW joints

Sample	YS (MPa)	UTS (MPa)	El (%)
BM	357 ± 4	447 ± 4	10.7 ± 1.2
300–200	237 ± 1	301 ± 7	5.1 ± 0.9
300–400	240 ± 1	311 ± 2	7.0 ± 0.2

UTS stands for ultimate tensile strength, YS stands for yield strength, and El stands for elongation

The hardness discrepancy phenomenon in the TMAZ of two joints was caused by the different heat inputs under different welding speeds. At a lower welding speed of 200 mm/min, 300–200 sample experienced a longer thermal history, resulting in the severe softening in the TMAZ due to the occurrence of the DRX and obvious precipitates coarsening (Figs. 4b and 5c). Usually, the hardness value in the TMAZ and HAZ can be improved as increasing the welding speed, due to the shortened thermal history [40]. Therefore, the hardness value was improved in the 300–400 sample under a higher welding speed of 400 mm/min.

The static tensile properties of the BM and BT-FSW joints are shown in Table 2. A high ultimate tensile strength (UTS) of 447 MPa was obtained in the BM. As the welding speed increasing from 200 to 400 mm/min, the tensile strength increased from 301 to 311 MPa. Meanwhile, the tensile fracture location indicated two different failure modes

for the BT-FSW joints, as shown in Fig. 7. Most samples failed along the border between the TMAZ and NZ, which is a regular fracture phenomenon for a FSW joint [41, 42, 42, 43]. However, some samples of the 300–200 joint failed along the JLR in the NZ (Fig. 7a), resulting in a bigger error value of the UTS due to the abnormal fracture. Previous researchers found that the JLR was characterized as a high-density Al_2O_3 particles formed during FSW [12, 29, 44, 45]. Tao et al. [29] found the conventional FSW joint failed along the JLR, leading to significantly reduced ductility. Meanwhile, the bonding strength at the JRL of 300–200 joint may be weakened at a lower welding speed of 200 mm/min, due to the longer thermal history. Therefore, there should be a certain competition in the fracture location between JLR and the border of TMAZ and NZ with similar bonding strength. However, the bonding strength at the JLR of 300–400 joint can be improved at a higher welding speed of 400 mm/min due to the shorter thermal history, which inhibits the abnormal fracture at the JRL (Fig. 7b).

3.2 High-Cycle Fatigue Properties

The maximum stress-number of cycles to failure (*S–N*) curves of the BM and BT-FSW joints is shown in Fig. 8. The BM has a relatively high fatigue strength of 140 MPa; however, the fatigue strength of both the 300–200 and 300–400 joints decreased to 110 MPa (78% of BM). The relationship between the maximum stress and number of cycles to failure under the condition of HCF can be fitted by the following Basquin equation [2, 46–49]:

$$\sigma_a = \sigma_f'(2N_f)^b$$

where N_f and σ_a represent fatigue life and applied stress, respectively. The σ_f' refers to fatigue strength coefficient, while b is fatigue strength exponent, which is associated with the initial microstructure stability.

Usually, the fatigue strength is decided by both of the σ_f' value and b value according to the Basquin equation. From the fitting lines in Fig. 8 and calculated values in Table 3, the BM exhibited the highest σ_f' value and b value, so a high fatigue strength of 140 MPa was achieved. The σ_f' value of 300–200 joint slightly decreased compared to that of the BM, but the b value decreased clearly to − 0.176. On the other hand, a smaller σ_f' value (1396 MPa) and a larger b value (− 0.156) were obtained in 300–400 joint compared to that of the 300–200 joint. Based on the comprehensive influence of the σ_f' and b values, the same fatigue strength of 110 MPa was finally achieved in both BT-FSW joints.

Figure 9 compares the fatigue strength and tensile strength of the BT-FSW joints in this study with other 2xxx series Al alloy joints in previous studies [1, 49–53]. In this study, the fatigue life up to 10^7 cycles was specified as the fatigue limit, and some data were derived and calculated according to the previous results in the literature. It is clear that the fatigue strength was usually lower than 100 MPa for the joints of 2xxx series Al alloys [2, 50, 52]. The fatigue strength of the BT-FSW joints in this study was obviously higher than those of other 2219 Al alloy joints, including the conventional FSW joints. Franchim et al. [53] obtained a FSW joint of 2024 Al alloy with a high fatigue strength of 112 MPa (estimated from the fatigue data), but its tensile strength was as high as 445 MPa. Therefore, enhanced fatigue strengths were obtained in the BT-FSW joints of 2219 Al alloy, and the fatigue ratio (fatigue strength/tensile strength) was as high as 0.365 in 300–200 sample.

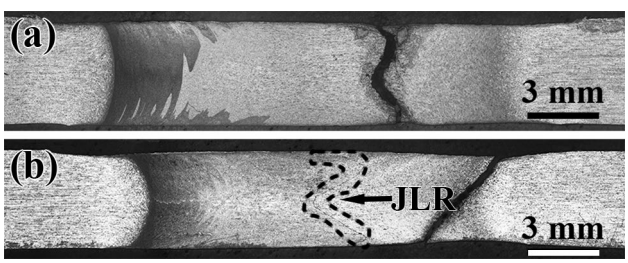

Fig. 7 Tensile fracture locations of BT-FSW joints under welding speeds of **a** 200 mm/min, **b** 400 mm/min

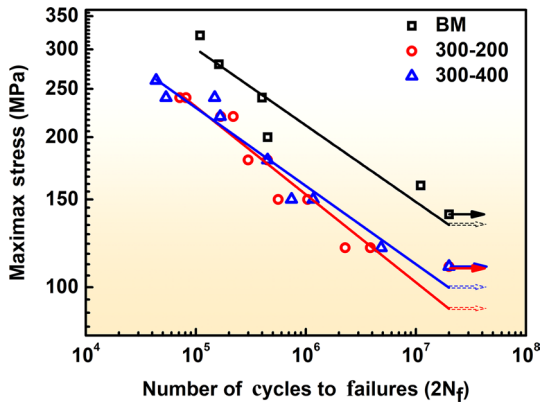

Fig. 8 Log–log form stress–fatigue life (S–N) curves for BM and BT-FSW joints

Table 3 Fatigue properties of BM and BT-FSW joints

Sample	Fatigue strength (MPa)	Fatigue ratio	σ_f'(MPa)	b value
BM	140	0.313	1760	− 0.154
300–200	110	0.365	1752	− 0.176
300–400	110	0.354	1396	− 0.156

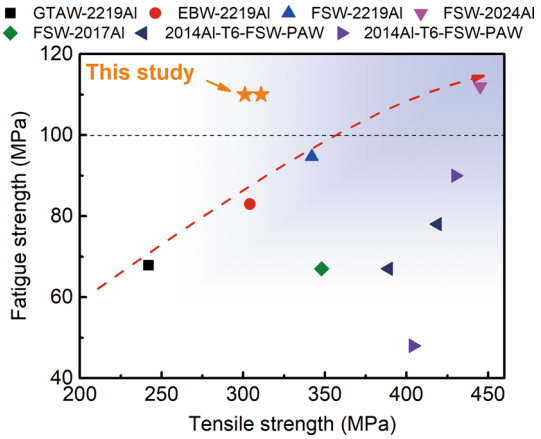

Fig. 9 Fatigue strength and tensile strength of various 2xxx series Al alloy joints [2, 50, 52, 53]

3.3 Fatigue Fracture Behavior

Figure 10 shows the typical morphologies of fracture locations for the BT-FSW joints under different maximum cyclic stresses. It is interesting that the fracture behavior of the fatigue samples was different from that of the tensile samples. During the HCF tests, no samples failed at the JLR even for the 300–200 joint whose fracture locations are at the TMAZ (Fig. 10a) or near the boundary between the NZ and TMAZ (Fig. 10b). During the fatigue tests, the applied stress was lower than the tensile strength, especially for the condition of longer fatigue life. In this case, the bonding strength at the JLR was larger than the applied stress during the HCF tests, so no preferential fractures occurred at the JLR. The TMAZ of the 300–200 joint with the lowest hardness values on both AS and RS became the weakest zone and fractured preferentially under the cyclic stress. As the welding speed increased to 400 mm/min, the LHZ was located at the NZ, so the 300–400 samples randomly failed at the NZ with the lowest hardness values, as shown in Fig. 10c and d.

Figure 11 shows the typical fracture morphologies of the BM after fatigue test at a maximum stress of 200 MPa. Three characteristic areas can be observed from Fig. 11a according to the different morphologies: crack initiation zone (I zone), stable crack propagation zone (II zone), and final fracture zones (III zone). It can be seen that the crack initiation zone was relatively flat due to the repeated friction of fracture surfaces (Fig. 11b). After crack initiation, the crack propagated in the mode of transgranular fracture, and there were a lot of fatigue striations, river patterns, and cleavage steps in the crack propagation zone (Fig. 11c). Further, a large number of secondary cracks perpendicular to the propagation direction of the main crack were observed, which were conducive to the improvement of fatigue performance. There are a lot of dimples in the final fracture zone (Fig. 11d), which belongs to the conventional micropore aggregation fracture.

Figure 12 shows the typical fracture morphologies of the 300–200 joint after fatigue test under a maximum stress of 120 MPa, which fractured at the TMAZ. It is found that the crack initiation site was at the sample corner, and similar morphology was achieved in the crack initiation zone to that of the BM (Fig. 12a and b). Transgranular fracture was also

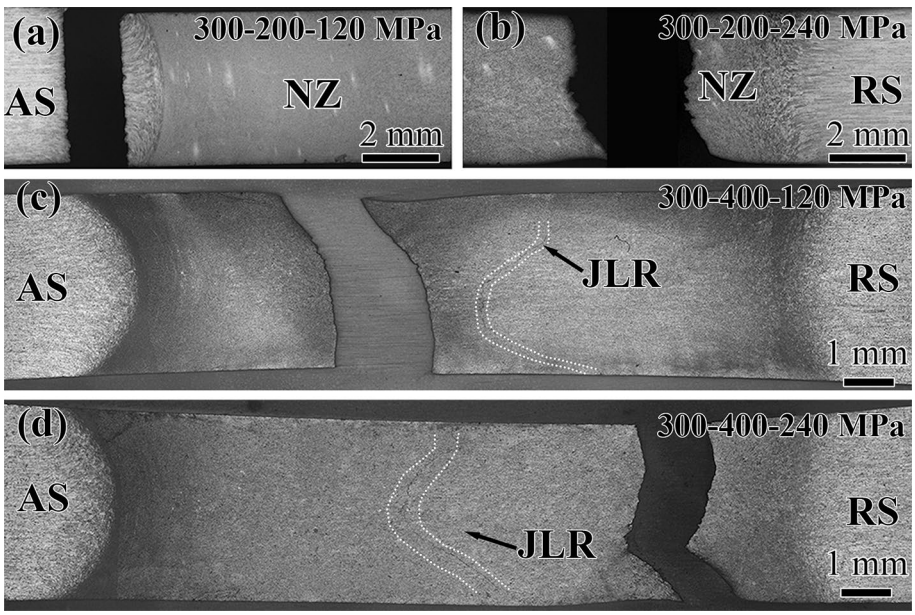

Fig. 10 Cross section fracture morphologies of BT-FSW joints under different maximum stress: **a** 300–200-120 MPa, **b** 300–200-240 MPa, **c** 300–400-120 MPa, **d** 300–400-240 MPa

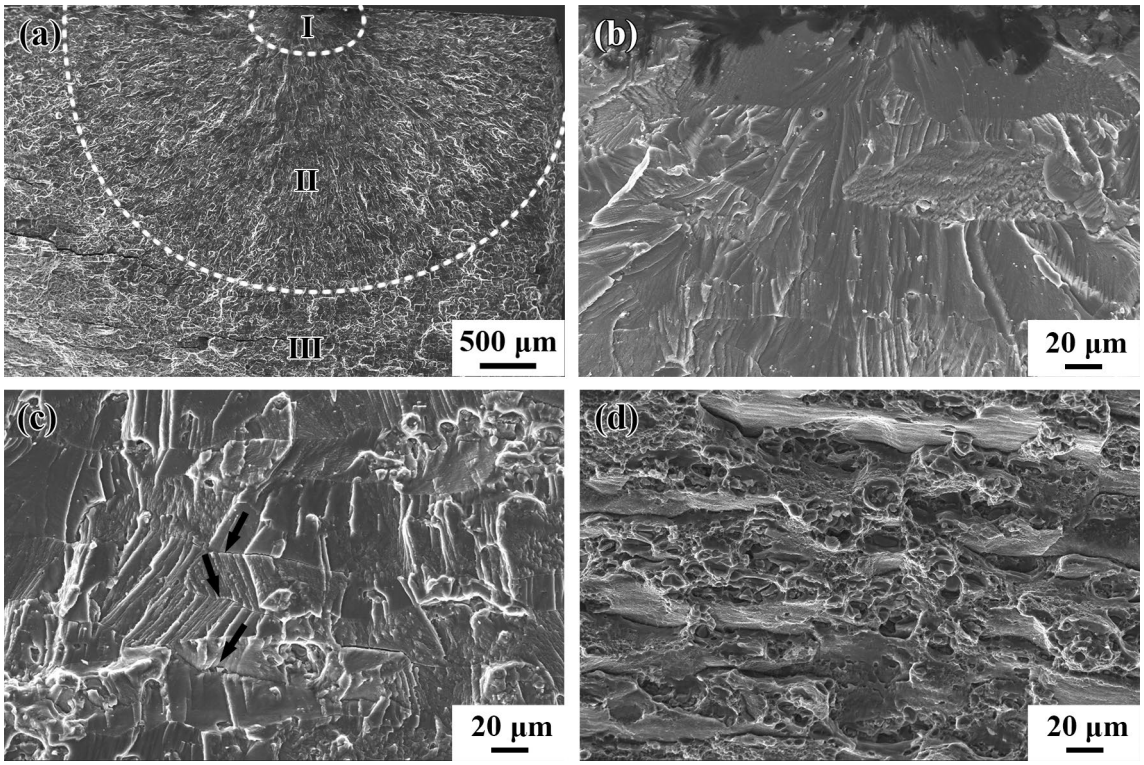

Fig. 11 Fracture surface morphologies of BM at a maximum stress of 200 MPa: **a** low magnification overview, **b** crack initiation zone, **c** crack propagation zone, **d** final fracture zone

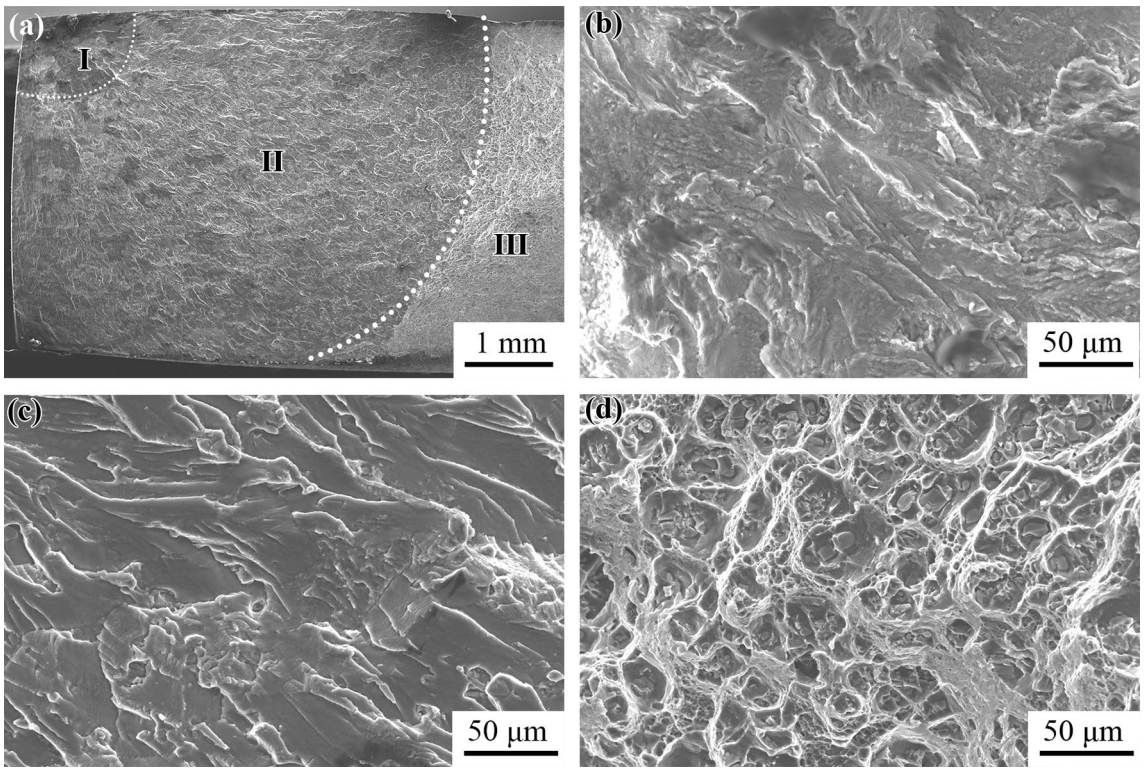

Fig. 12 Fracture surface morphology of sample 300–200 at a maximum stress of 120 MPa: **a** low magnification overview, **b** crack initiation zone, **c** crack propagation zone, **d** final fracture zone

the main fracture mode, but the cleavage characteristic was not obvious compared to that of the BM (Fig. 12c). In the final fracture zone, dimples were the main fracture morphology, but the dimples were more uniform than that of the BM (Fig. 12d), due to the more equiaxed grains after DRX.

Figure 13 shows the typical fracture morphologies of the 300–400 joint after fatigue test under a maximum stress of 120 MPa, which fractured at the NZ. The crack initiation occurred near the corner of the NZ, and it was composed of many sugar-like fracture surface (Fig. 13b). The presence of oxide particles and impurities in the welding process may lead to crack initiation on the surface of the welded joint [22]. However, no cluster of oxide particles was observed on the fracture surface, and the size of the sugar-like structure was nearly equal to the grain size. Therefore, intergranular fracture was the main fracture mode in the crack initiation zone. The crack propagation zone consisted of a large number of fatigue striations, which are typical fatigue fracture characteristics of a metal with uniform microstructures (Fig. 13c). A large number of dimples were formed in the final fracture zone (Fig. 13d), and the size decreased clearly compared to that of the 300–200 joint.

The fatigue performance and fracture mechanism of the Al alloy joint were affected by welding parameters (e.g., tool geometry or welding speed), volumetric defects (e.g., weld flaws or JLRs), and intrinsic properties (e.g., material microstructure characteristics) [54]. Based on the above results, excellent HCF properties were obtained for both BT-FSW joints in this study, especially for the 300–400 joint under a higher welding speed of 400 mm/min which exhibited both high tensile strength and fatigue strength. Most of the 300–200 fatigue samples failed at the TMAZ during the HCF test, which is due to the coarsened grains and precipitates, but all of the 300–400 fatigue samples randomly failed at the NZ due to the improved hardness value in the TMAZ. The root flaw is usually connected with JLRs, which is fatal to the fatigue performance of the FSW joints as a crack initiation site [22–27]. Due to the unique characteristics of BT-FSW, no root flaws were formed, which usually appeared in conventional FSW joints. Therefore, the fatigue crack did not initiate and propagate along the JLR even if the sample fractured at the NZ, resulting in the excellent HCF properties.

4 Conclusions

In the present investigation, 4-mm-thickness 2219-T87 Al alloy plates were subjected to BT-FSW under relatively high welding speeds of 200 and 400 mm/min. The

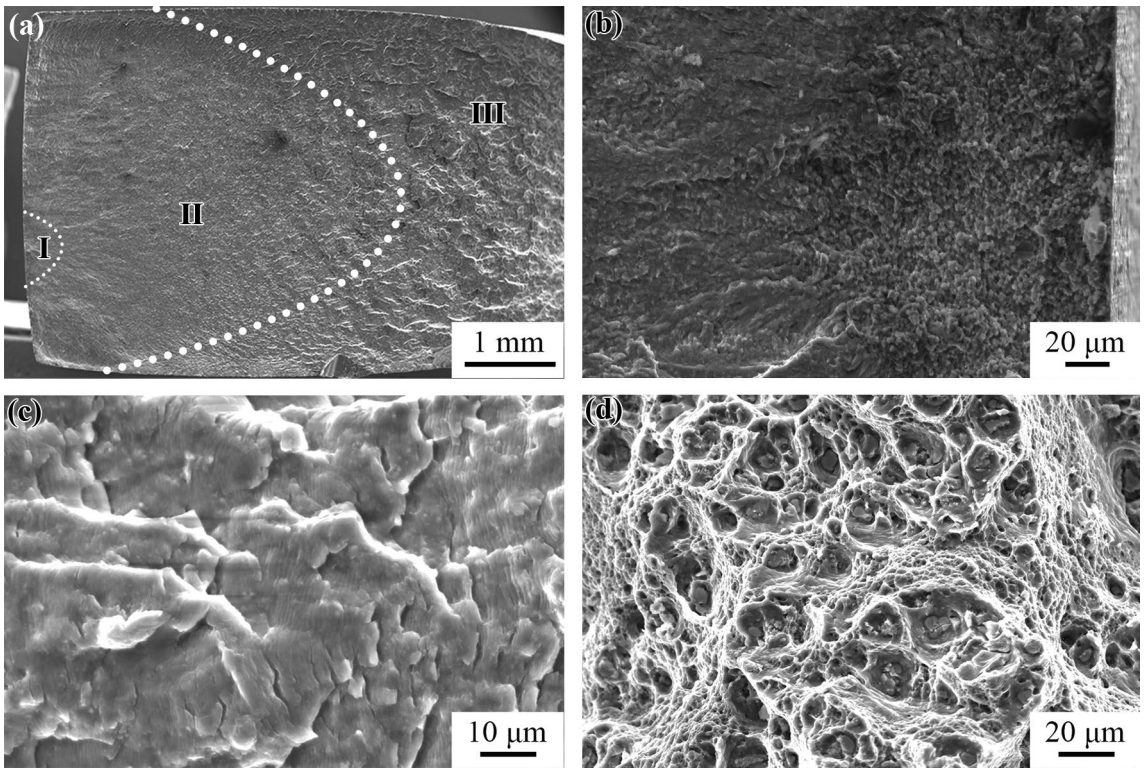

Fig. 13 Fracture surface morphology of sample 300–400 at a maximum stress of 120 MPa: **a** low magnification overview, **b** crack initiation zone, **c** crack propagation zone, **d** final fracture zone

microstructures, static mechanical properties, and HCF properties were carefully analyzed. The main conclusions can be summarized as follows:

1. No obvious defects were found in the BT-FSW joints, and finer grain microstructure was obtained in the NZ and HAZ with increasing the welding speed to 400 mm/min.

2. With increasing the welding speed from 200 to 400 mm/min, the tensile strength of the BT-FSW joints increased from 301 to 311 MPa. Though some 300–200 tensile samples failed at the JLR, most of the samples failed at the NZ or the border between NZ and TMAZ.

3. Enhanced fatigue strength of 110 MPa was obtained in both BT-FSW joints compared to other joints of 2xxx series Al alloys, which was attributed to the elimination of the root flaws by the lower shoulder, and the fatigue ratio was as high as 0.365 for 300–200 joint.

4. The fatigue fracture locations depended on the welding parameters, and most of the 300–200 samples failed at the TMAZ during HCF test, which is due to the coarsened grains and precipitates. However, all of the 300–400 samples randomly failed at the NZ due to the improved hardness value in the TMAZ at a higher welding speed.

Acknowledgements This work was financially supported by the LiaoNing Revitalization Talents Program under grant No. XLYC2002099, the LiaoNing Province Excellent Youth Foundation (No. 2021-YQ-01), the Youth Innovation Promotion Association of the Chinese Academy of Sciences (No. Y2021061), and the IMR Innovation Fund (No. 2022-PY11).

Declarations

Conflict of interest The authors state that there are no conflicts of interest to disclose.

References

[1] S. Malarvizhi, V. Balasubramanian, Mater. Des. **32**, 1205 (2011)
[2] S. Malarvizhi, V. Balasubramanian, Weld. World **56**, 105 (2012)
[3] H. Zhang, M. Wang, X. Zhang, G. Yang, Mater. Des. **65**, 559 (2015)
[4] F.F. Wang, W.Y. Li, J. Shen, Q. Wen, J.F. dos Santos, J. Mater. Sci. Technol. **34**, 135 (2018)
[5] X. Meng, Y. Huang, J. Cao, J. Shen, J.F. dos Santos, Prog. Mater Sci. **115**, 100706 (2021)
[6] J.C. Hou, H.J. Liu, Y.Q. Zhao, Int. J. Adv. Manuf. Technol. **73**, 1073 (2014)
[7] C. Yang, D.R. Ni, P. Xue, B.L. Xiao, W. Wang, K.S. Wang, Z.Y. Ma, Mater. Charact. **145**, 28 (2018)
[8] Y. Xie, X. Meng, F. Wang, Y. Jiang, X. Ma, L. Wan, Y. Huang, Corros. Sci. **192**, 109800 (2021)
[9] X. Ma, Y. Xie, X. Meng, H. Chen, F. Wang, Y. Jiang, L. Wan, Y. Huang, Sci. Technol. Weld. Join. **26**, 599 (2021)
[10] F.C. Liu, Z.Y. Ma, Metall. Mater. Trans. A **39**, 2378 (2008)
[11] F.F. Wang, W.Y. Li, J. Shen, Z.H. Zhang, J.L. Li, J.F. dos Santos, Sci. Technol. Weld. Join. **21**, 479 (2016)
[12] F.F. Wang, W.Y. Li, J. Shen, S.Y. Hu, J.F. dos Santos, Mater. Des. **86**, 933 (2015)
[13] M. Ericsson, R. Sandstrom, Int. J. Fatigue **25**, 1379 (2003)
[14] S. Kainuma, H. Katsuki, I. Iwai, M. Kumagai, Int. J. Fatigue **30**, 870 (2008)
[15] C. Zhou, X. Yang, G. Luan, Mater. Sci. Eng. A **418**, 155 (2006)
[16] C. Zhou, X. Yang, G. Luan, J. Mater. Sci. **41**, 2771 (2006)
[17] Y. Hu, H. Liu, D. Li, J. Mater. Sci. Technol. **85**, 205 (2021)
[18] Y.S. Sato, F. Yamashita, Y. Sugiura, S.H.C. Park, H. Kokawa, Scr. Mater. **50**, 365 (2004)
[19] R.P. Mahto, C. Gupta, M. Kinjawadekar, A. Meena, S.K. Pal, J. Manuf. Processes **38**, 370 (2019)
[20] Y.S. Sato, H. Takauchi, S.H.C. Park, H. Kokawa, Mater. Sci. Eng. A **405**, 333 (2005)
[21] V. Malik, S.V. Kailas, J. Mater. Process. Technol. **258**, 80 (2018)
[22] C. Vidal, V. Infante, J. Mater. Eng. Perform. **23**, 1340 (2014)
[23] T.L. Dickerson, J. Przydatek, Int. J. Fatigue **25**, 1399 (2003)
[24] C. Zhou, X. Yang, G. Luan, Scr. Mater. **53**, 1187 (2005)
[25] M. Kadlec, R. Ruzek, L. Novakova, Int. J. Fatigue **74**, 7 (2015)
[26] S.S. Di, X.Q. Yang, D.P. Fang, G.H. Luan, Mater. Chem. Phys. **104**, 244 (2007)
[27] S.S. Di, X.Q. Yang, G.H. Luan, B. Jian, Mater. Sci. Eng. A **435**, 389 (2006)
[28] T. Le Jolu, T.F. Morgeneyer, A. Denquin, A.F. Gourgues-Lorenzon, Int. J. Fatigue **70**, 463 (2015)
[29] Y. Tao, Z. Zhang, D.R. Ni, D. Wang, B.L. Xiao, Z.Y. Ma, Mater. Sci. Eng. A **612**, 236 (2014)
[30] M. Liang, H. Zhang, L. Zhang, P. Xue, D. Ni, W. Wang, Z. Ma, H. Ye, Z. Yang, Acta Metall. Sin. Engl. Lett. **34**, 12 (2020)
[31] Y.F. Wang, J. An, K. Yin, M.S. Wang, Y.S. Li, C.X. Huang, Acta Metall. Sin. -Engl. Lett. **31**, 878 (2018)
[32] G.K. Padhy, C.S. Wu, S. Gao, J. Mater. Sci. Technol. **34**, 1 (2018)
[33] R.S. Mishra, Z.Y. Ma, Mater. Sci. Eng. R **50**, 1 (2005)
[34] F.C. Liu, Y. Hovanski, M.P. Miles, C.D. Sorensen, T.W. Nelson, J. Mater. Sci. Technol. **34**, 39 (2018)
[35] Z. Zhang, B.L. Xiao, Z.Y. Ma, J. Mater. Sci. **47**, 4075 (2012)
[36] W. Xu, Y. Luo, W. Zhang, M. Fu, J. Mater. Sci. Technol. **34**, 173 (2018)
[37] C.S. Paglia, R.G. Buchheit, Mater. Sci. Eng. A **429**, 107 (2006)
[38] P.B. Srinivasan, K.S. Arora, W. Dietzel, S. Pandey, M.K. Schaper, J. Alloys Compd. **492**, 631 (2010)
[39] Z.L. Wang, Z. Zhang, P. Xue, D.R. Ni, Z.Y. Ma, Y.F. Hao, Y.H. Zhao, G.Q. Wang, Mater. Sci. Eng. A **832**, 138953 (2022)
[40] C. Wang, B.B. Wang, D. Wang, P. Xue, Q.Z. Wang, B.L. Xiao, L.Q. Chen, Z.Y. Ma, Acta Metall. Sin. -Engl. Lett. **32**, 677 (2019)
[41] F. Qiang, W. Wang, K. Qiao, P. Peng, T. Zhang, X.H. Guan, J. Cai, Q. Meng, H.X. Zhao, K.S. Wang, Acta Metall. Sin. -Engl. Lett. **35**, 1329 (2022). https://doi.org/10.1007/s40195-022-01373-y
[42] P. Zhu, L. Zhang, Z. Li, K.H. Lo, J. Wang, Y. Sun, S. Guan, Acta Metall. Sin. -Engl. Lett. **35**, 1079 (2022). https://doi.org/10.1007/s40195-021-01358-3
[43] Z.W. Wang, J.F. Zhang, G.M. Xie, L.H. Wu, H. Zhang, P. Xue, D.R. Ni, B.L. Xiao, Z.Y. Ma, J. Mater. Sci. Technol. **102**, 213 (2022)
[44] Y. Tao, Z. Zhang, P. Xue, D.R. Ni, B.L. Xiao, Z.Y. Ma, J. Mater. Sci. Technol. **123**, 92 (2022)
[45] G.H. Li, L. Zhou, S.F. Luo, Z.Y. Du, J.C. Feng, F.X. Meng, Sci. Technol. Weld. Joining **25**, 142 (2019)
[46] Y. Tao, D.R. Ni, B.L. Xiao, Z.Y. Ma, W. Wu, R.X. Zhang, Y.S. Zeng, Mater. Sci. Eng. A **693**, 1 (2017)
[47] X.H. An, S.D. Wu, Z.G. Wang, Z.F. Zhang, Prog. Mater Sci. **101**, 1 (2019)
[48] X.H. An, Q.Y. Lin, S.D. Wu, Z.F. Zhang, Mater. Res. Lett. **3**, 135 (2015)
[49] B.B. Wang, P. Xue, B.L. Xiao, W.G. Wang, Y.D. Liu, Z.Y. Ma, Sci. Technol. Weld. Joining **25**, 81 (2019)

[50] S. Malarvizhi, V. Balasubramanian, J. Mater. Eng. Perform. **20**, 359 (2011)
[51] O. Mimouni, R. Badji, A. Kouadri-David, R. Gassaa, N. Chekroun, M. Hadji, Trans. Indian Inst. Met. **72**, 1853 (2019)
[52] S. Malarvizhi, V. Balasubramanian, Trans. Nonferrous Met. Soc. **21**, 962 (2011)
[53] H. Aydin, M. Tutar, A. Durmus, A. Bayram, T. Sayaca, Trans. Indian Inst. Met. **65**, 21 (2012)
[54] A.S. Franchim, F.F. Fernandez, D.N. Travessa, Mater. Des. **32**, 4684 (2011)
[55] I. Vysotskiy, S. Malopheyev, S. Rahimi, S. Mironov, R. Kaibyshev, Mater. Sci. Eng. A **760**, 277 (2019)